Chinese Journal of
POLYMER SCIENCE

RESEARCH ARTICLE

https://doi.org/10.1007/s10118-023-2924-4
Chinese J. Polym. Sci. **2023**, *41*, 1238–1249

A Multi-model, Large-range Flexible Strain Sensor Based on Carbonized Silk Habotai for Human Health Monitoring

Shi-Dong Ma[a], Yu-Ting Wu[a], Jian Tang[a], Yu-Min Zhang[a], Tao Yan[a,b*], and Zhi-Juan Pan[a,b*]

[a] *College of Textile and Clothing Engineering, Soochow University, Suzhou 215123, China*
[b] *National Engineering Laboratory for Modern Silk, Suzhou 215123, China*

Electronic Supplementary Information

Abstract In recent years, flexible strain sensors have received considerable attention owing to their excellent flexibility and multifunctionality. However, it is still a great challenge for them to accurately monitor multi-model deformations with high sensitivity and linearity. In this study, the industrial insulating silk habotai was successfully converted into carbonized silk habotai (CSH) for use in strain sensors. A strain sensor created using CSH exhibited excellent sensing performance under multi-model deformations, including stretching, twist and bending. The maximum tensile strain was 434%. The gauge factors were 14.6 in the wide tensile range of 0%–400% with a high linearity of 0.959. In addition, the CSH strain sensor exhibited an extremely fast response time (110 ms) and could accurately detect bending (0°–180°) and torsional (0°–180°) strains. High durability and repeatability were observed for the multi-model strains. Finally, a new type of smart pillow was developed to accurately record head movement and breathing during sleep. The sensor may also be used for auxiliary training in table tennis. The proposed CSH strain sensor has shown great potential for applications in smart devices and human-machine interactions.

Keywords Carbonized silk habotai; Strain sensor; Smart pillow; Human motions

Citation: Ma, S. D.; Wu, Y. T.; Tang, J.; Zhang, Y. M.; Yan, T.; Pan, Z. J. A multi-model, large-range flexible strain sensor based on carbonized silk habotai for human health monitoring. *Chinese J. Polym. Sci.* **2023**, *41*, 1238–1249.

INTRODUCTION

With the development of science and technology, wearable electronic devices have received considerable attention.[1,2] As an important part of wearable electronic devices, flexible strain sensors are widely used in intelligent robot design,[3] human motion detection,[4] personalized human-machine interaction,[5] digital health monitoring, and other fields. Flexible strain sensors can be divided on the basis of their sensing mechanisms into resistance,[6–8] capacitive,[9–11] voltage (piezoelectric[12,13] and triboelectric[14,15]), inductance[16] and magnetism.[17] Resistance strain sensors[18,19] convert the strain into a variation in electron transport capacity through structural transformation of a flexible conductive network. Owing to their relatively simple preparation process, ease of use, high flexibility, and superior sensitivity, they have received extensive attention from researchers.[20,21]

Common conductive materials include carbon nanomaterials (including graphene,[22] carbon nanotubes,[23] and carbon black[24]), metal nanomaterials,[25,26] and conductive polymers.[27–29] Although conductive materials can successfully establish conductive networks, their sensing performances are not outstanding. The manufacturing processes of strain sensors made of nanomaterials and conducting polymers are often expensive and lacking in environmental friendliness. Therefore, the fabrication of sensors with environmentally friendly and cost-effective processes is highly anticipated. Carbon-based conductive materials obtained from natural materials can effectively solve the above problems.[30,31]

Silk fibroin, the main component of silk, can be converted into conductive bio-derived carbon materials by simple heat treatment. Carbonized silk has outstanding electrical conductivity and may be an environmentally friendly conductive material.[32–34] In addition, researchers have found that different carbonization processes affect the electrical conductivity and mechanical properties of silk fabrics,[35–37] which will further affect the performance of silk-based flexible strain sensors silk fibers carbonized at a low-temperature exhibit a low graphitization degree and poor conductivity, resulting in unsatisfactory sensitivity.[38] At a high temperature, carbonized silk fibers will be brittle and significantly reduced mechanical properties, resulting in low conductivity and stretching properties,[39] leading to poor strain sensing performance. Besides, the properties of carbonized silk were also affected by the heating process. The carbonized silk prepared by the one-step heating method exhibited superior electrical conductivity.[40] The carbonized silk prepared by the gradient heating

* Corresponding authors, E-mail: yantao@suda.edu.cn (T.Y.)
E-mail: zhjpan@suda.edu.cn (Z.J.P)

Received November 7, 2022; Accepted December 7, 2022; Published online February 10, 2023

method exhibited higher mechanical properties.[41] To the best of our knowledge, no study has compared different carbonized silk processes or explored any of them in greater detail.

Researchers have carbonized various natural fibers in a previous study to obtain strain sensors.[42–46] By comparison, it was found that the silk-based strain sensors exhibited more outstanding sensing performance.[47] The carbonized georgette strain sensor had been shown to possess excellent sensitivity (GF of 29.7 within 40% strain and 173.0 for a strain of 60%–100%). Friction between the curly yarn and the elastic matrix further aggravates yarn breakage.[48] Thus its tensile strain was only 110%,[49] which could not meet the demand of high tensile strain monitoring in daily life. To improve this weakness, Wang *et al*.[50] carbonized plain silk fabrics without twist in weft yarns to fabricate flexible strain sensors. The maximum tensile strain of the flexible sensor was greater than 500%, but the GF was only 9.6. Furthermore, the sensor could only realize the draft strain monitoring, and the response of the sensor in other strain models was not sensed. The sensing performance was divided into multiple linear segments during the whole strain range, which did not facilitate the application of the sensor and the continuity of the sensor linearity. By analyzing the structure (plain, twill and satin) of the fabric strain sensor, they found that the plain silk fabric sensors had the maximum stretching strain. Despite their encouraging progress in this field, the strain sensors which provide only single strain model detection cannot meet the daily exercise needs of the human body.[51] Therefore, researchers have proposed more precise requirements for the strain models and linearity of flexible strain sensors.

In this study, a non-conductive habotai, an insulating material commonly used in industry, was applied as a carbonized silk material. The optimal carbonization scheme was determined by exploring the properties of carbonized silk habotais (CSHs) under different carbonization processes and temperatures, and a flexible strain sensor was successfully fabricated using CSH. We discuss the resistive responses of CSH strain sensors under a multi-model strain, which had a clear linear relationship and significantly different sensing results. Outstanding stability was obtained under different loading models and strain ranges. The working mechanism of the CSH strain sensors under multi-model strain was revealed. The CSH strain sensor was successfully applied to a smart pillow for the first time, allowing accurate monitoring of the sleep status of the human body. We also successfully demonstrated its potential application in table tennis training. We believe that our multi-model strain sensors will open new avenues for health monitoring and human motion detection, which is expected to promote the development of next-generation healthcare and human-machine interconnection.

EXPERIMENTAL

Materials

Habotai (silk plain-weave) was supplied by Huajia Co. Ecoflex Supersoft 0030 was purchased from Smooth-on, Inc. Cu wire was provided by Runde Metal Materials Co., Ltd., and conductive silver paint was obtained from SPI Supplies Division Structure Probe Inc.

Fabrication of CSHs

Habotai was cleaned with deionized water by ultrasonication for 1 h and dried at 40 °C for 6 h. The clean habotai was placed in a tube furnace for carbonization, and the generated CSHs were cut into 1 cm × 5 cm rectangles. Five types of CSHs, CSH_1, CSH_2, CSH_3, CSH_4 and CSH_5, were prepared using different carbonization processes, as shown in Table 1, to discuss the effects of the heating rate, heating temperature, and gradient heating process on their sensing performance.

Preparation of CSH Strain Sensors

Equal parts of liquid Ecoflex A and B were mixed in a container. One gram of the mixture was dropped onto a glass sheet. The bubbles in the solution were extracted by vacuum and then dried for 2 h in a 60 °C blast oven to obtain a uniform Ecoflex film. The CSH was placed on the film, and both ends were fixed with a copper wire and coated with conductive silver glue to form two electrodes. A layer of 1 g of Ecoflex mixture was applied to the upper layer of the sensor, and the process of vacuum extraction and oven drying was repeated. Finally, the sensor was kept stationary in the environment for 48 h to eliminate internal stress. The preparation process is illustrated in Fig. 1(a). Figs. 1(b) and 1(c) show that although the thickness of the sensor was 1.12 mm, it still exhibited good flexibility and could be bent freely. The elastic matrix part appeared to be translucent.

Characterization

A scanning electron microscope (SEM, S8100, Hitachi, Japan) was used to observe the morphologies of the fabrics. Based on the SEM images, the yarn diameters of the different fabrics were measured using an image analysis software (Image-Pro Plus). A Raman spectrometer (LabRAM XploRA, HORIBA Scientific, France) with a wavelength of 532 nm was used to obtain the Raman spectra of the stabilized and carbonized habotai. The thickness and electrical resistance of the strain sensors were measured using a micrometer caliper (Kincrome Australia Pty Ltd.) and a multifunction digital four-probe tester (ST-2258C, Suzhou Jingge Electronic Co., Ltd.), respectively. X-ray photoelectron spectroscopy (XPS, K-Alpha Thermo Scientific, USA) was used to determine the chemical structure of the materials and for quantitative elemental analysis. X-ray diffraction (XRD, Bruker D8, Germany) was used to characterize the crystal structure and composition of the materials. Thermogravimetric analysis (TGA, SDT Q600) was used to reveal the difference in the kinetics and residual weight.

A universal testing machine (Instron 3365, Instron Corporation) was used to measure and analyze the mechanical and

Table 1 The carbonization processes for five kinds of CSHs.

Type	First stage heating interval (heating rate)	Holding time	Second stage heating interval (heating rate)	Holding time
CSH_1	20–900 °C (3 °C·min^{-1})	120 min	/	
CSH_2	20–900 °C (5 °C·min^{-1})	120 min	/	
CSH_3	20–350 °C (5 °C·min^{-1})	180 min	350–900 °C (3 °C·min^{-1})	120 min
CSH_4	20–350 °C (5 °C·min^{-1})	180 min	350–950 °C (3 °C·min^{-1})	120 min
CSH_5	20–350 °C (5 °C·min^{-1})	180 min	350–1000 °C (3 °C·min^{-1})	120 min

https://doi.org/10.1007/s10118-023-2924-4

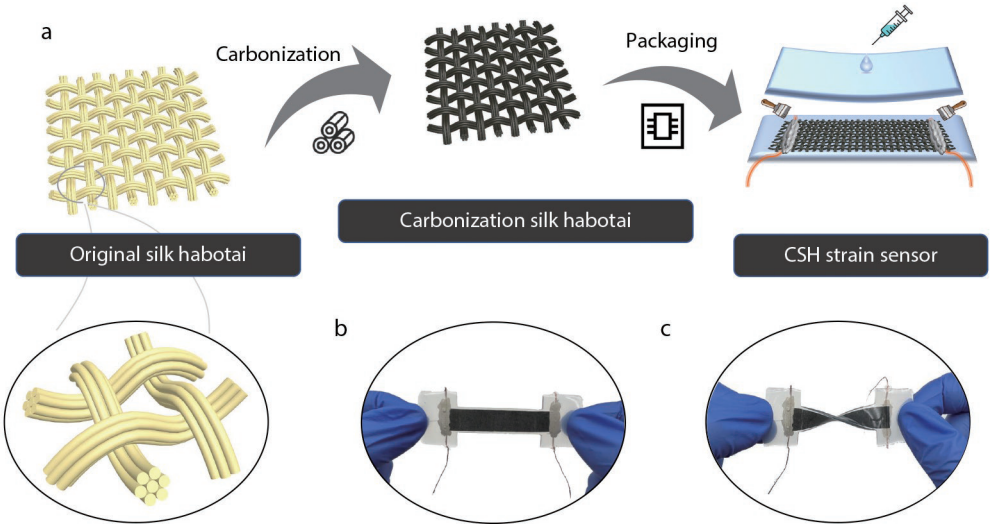

Fig. 1 (a) Schematic diagram of the preparation process of CSH strain sensor. Actual photos for (b) the CSH strain sensor and (c) the twisting sensor.

sensing properties of the flexible strain sensors. A flexible resistance tester (Prtronic FT2000, China) was used for bending, torsional, and cyclic testing. The strain sensor was fixed on a universal testing machine and the clamping distance was set to 30 mm. An electrochemical workstation (CHI 760E, CH Instruments Inc., USA) was used to record the electrical signals using the *I-t* curve under a 0.1 V constant voltage. The time interval between the adjacent data output of the universal testing machine and electrochemical workstation was 0.1 s. The GF value was defined to represent the tensile sensitivity of the strain sensors, and was calculated according to Eq. (1):

$$\mathrm{GF} = \frac{\Delta R/R_0}{\Delta L/L_0} \tag{1}$$

where ΔR is the absolute value of the difference between the final resistance R and the initial resistance R_0, and ΔL is the absolute value of the difference between the final length L and the initial length L_0. The S_b value represented the bending sensitivity of the strain sensor. S was calculated using Eq. (2):

$$S_b = \frac{\Delta R/R_0}{\theta} \tag{2}$$

where ΔR is the absolute value of the difference between the final resistance R and the initial resistance R_0, and θ is the bending angle. The S_t value represented the twisting sensitivity of the strain sensor, and was calculated using Eq. (3):

$$S_t = \frac{\Delta R/R_0}{\theta} \tag{3}$$

where θ is the twisting angle.

RESULTS AND DISCUSSION

Preparation and Characterization of CSHs

The carbonization process of habotai is relatively simple, but there are various types of processes. In the introduction of this article, we mentioned three carbonization processes that were the most commonly used, which also contrast sharply with each other.

Fig. 2(a) shows macro images of pristine habotai, CSH_1, CSH_2 and CSH_3. The pristine habotai was smooth and shiny, while it was evident that there were small bumps on the surface of CSH_1 and ripples on the surface of CSH_2; these were due to the rapid heating rate and uneven heating of the fabric as a whole. After pyrolysis, the surrounding area of the fabric shrank rapidly, and the middle area shrank slowly, thus presenting the problem of nonuniformity and insufficient carbonization shrinkage. The surface of CSH_3 was relatively flat, and CSH_3 still retained the shape of the pristine habotai. Compared with the initial habotai area, the areas of CSH_1, CSH_2 and CSH_3 shrank to 43.1%, 44.7% and 45.6%, respectively. Fig. 2(b) shows the SEM images of pristine habotai, CSH_1, CSH_2 and CSH_3. It can be observed that the CSH_1, CSH_2, and CSH_3 completely retain the characteristic structure of plain weave fabric, and the warp and weft yarns are not twisted. The yarn diameter after carbonization was significantly smaller than that of the pristine yarn (180.60 μm), with the average yarn diameters of CSH_1, CSH_2, and CSH_3 being 85.12, 84.39 and 88.67 μm, respectively. The heating rate of CSH_2 was high, and the interior of the fiber rapidly decomposed. To maintain the shape, the fiber was rapidly contracted and straightened by the internal stress. Therefore, a compact ordered graphitized structure was formed which helped to promote the electrical conductivity. The carbonization process of CSH_3 took a long time. Sufficient carbonization could better retain the morphology and structure of CSH_3. The average resistances of CSH_1, CSH_2 and CSH_3 as measured by a multifunction digital four-probe tester were 12.72, 11.37 and 11.69 Ω, respectively, as shown in Fig. S1 (in the electronic supplementary information, ESI). TGA test results are shown in Fig. S2(a) (in ESI). By analyzing TGA and DTG curves, it can be concluded that the thermal decomposition temperature of habotai is 303 °C, rapidly decomposed at 337 °C. When the temperature continued rising to 600 °C, the DTG curve tended to be flat. The quality of silk habotai no longer changed significantly and entered the thermal stability stage. In order to more precisely investigate the carbonization process of habotai at different ramp-up processes, TG experiments with ramp-up rates of 3 and 5 °C·min^{-1} were measured (Fig. S2b in

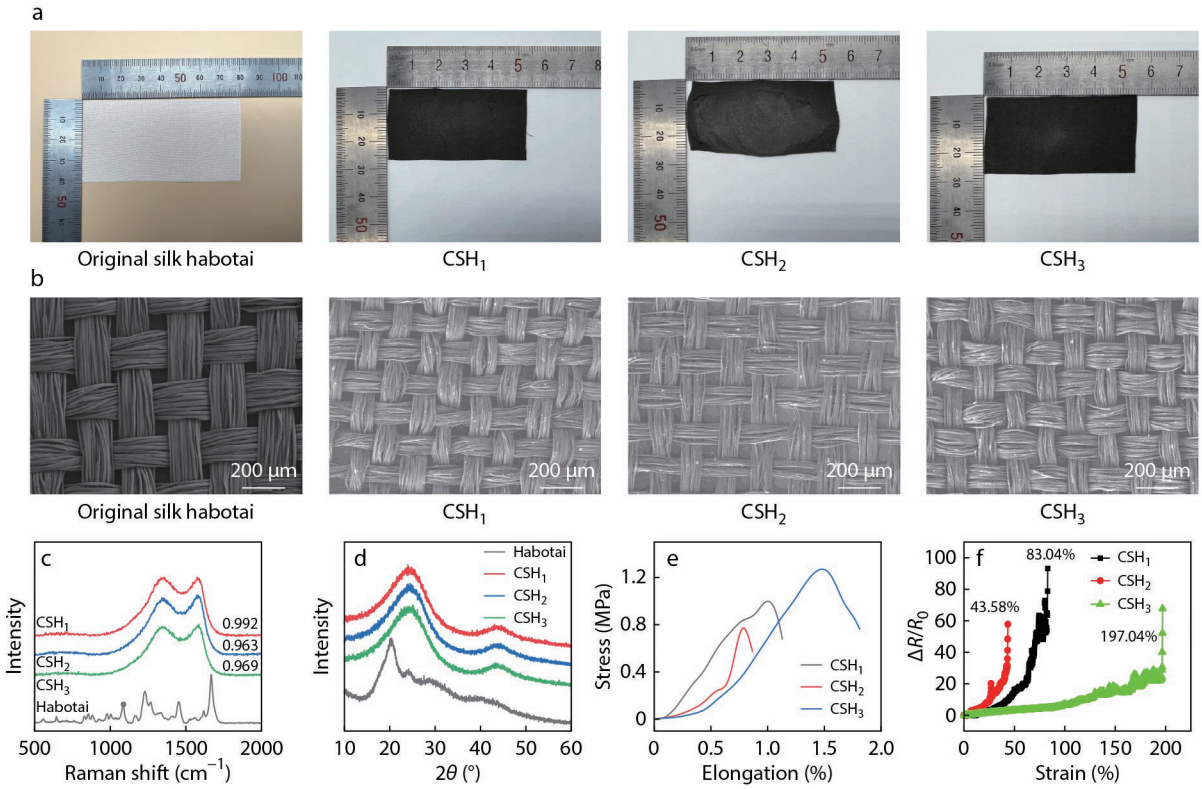

Fig. 2 (a) Photographs and (b) SEM images of pristine habotai, CSH_1, CSH_2 and CSH_3; (c) Raman spectra, (d) XRD patterns and (e) stress-strain diagrams of pristine habotai, CSH_1, CSH_2 and CSH_3; (f) The relative resistance changes of CSH_1, CSH_2 and CSH_3 strain sensors along the weft direction at a tensile rate of 60 mm·min^{-1}.

ESI). The results showed that the curves for the two rates overlapped until the temperature reached nearly 337 °C. At temperatures above 337 °C, the weight loss of the 3 °C·min^{-1} TG curve was more pronounced. The weight loss in the TG curve at 5 °C·min^{-1} tended to moderate. This was due to the slower heating rate and longer heating time, which gave CSH_1 and CSH_3 more sufficient time for the moderating pyrolysis process.

The microstructures of the pristine habotai and CSHs were studied using Raman spectroscopy, as shown in Fig. 2(c). The Raman spectra of pristine habotai show characteristic bands of silk fibroin at 827, 856, 884, 1085, 1228, 1267 and 1667 cm^{-1}. The Raman spectra of the CSHs show two distinct characteristic bands at 1350 and 1588 cm^{-1}, named the D-band and G-band, respectively.[52] The D-band is attributed to the existence of amorphous carbon and structural defects, while the G-band represents the stretching motion of sp^2 atoms in the carbon ring or long chain. The relative intensities of the D and G bands are denoted as I_D and I_G, respectively. The ratio of the D and G bands could be used to characterize the degree of transformation of the internal structure of habotai before and after carbonization. The I_D/I_G values for CSH_1, CSH_2 and CSH_3 were 0.992, 0.963 and 0.969, respectively; a lower I_D/I_G value indicates lower amorphous carbon content and a higher degree of graphitization. The high graphitization made it possible for the CSHs to be highly conductive and have lower resistance. CSH_1 having a higher I_D/I_G value than CSH_2 and CSH_3 explained the higher resistance of CSH_1.

XRD was carried out on the pristine habotai and CSHs to investigate the phase of the samples, as shown in Fig. 2(d). Pristine habotai shows the characteristic peaks near 23.89° and 28.80° and belonging to the α-helix structure. The characteristic peaks near 20.41° and 40.48° were β-folded structure diffraction peaks. CSH_1, CSH_2, and CSH_3 show wide amorphous peaks at 24° and 44°, corresponding to the (002) and (101) crystal planes of the graphite structure, respectively.[53] To further determine the carbonization degree of habotai, XPS characterization of CSH_1, CSH_2 and CSH_3 was used to obtain their relative elemental content (Fig. S3a in ESI). Table S1 (in ESI) illustrates that habotai contains C, N and O elements before and after carbonization. During the carbonization process, the macromolecular chains in the silk underwent cross-linking and polycondensation, accompanied by pyrolysis. Most of the O and N were released as gases. The remaining N was transformed into N substituents in the graphite layer or embedded in the carbon ring to form a stable carbon and nitrogen structure.[54] The remaining O was converted into O substituents in the graphite layer. CSH_1 has the highest carbon content among CSH_1, CSH_2 and CSH_3. With a steady increase in temperature, more N and O could be released to form N_2 and O_2. CSH_2 demonstrated the lowest C content because rapid heating does not play a positive role in the carbonization of habotai, resulting in insufficient carbonization of the material. The heat preservation environment of CSH_3 at 350 °C using the gradient heating method provided sufficient time for the formation of N and O substituents.

The mechanical properties of CSHs can be intuitively observed through tensile tests in the weft direction of CSHs with

https://doi.org/10.1007/s10118-023-2924-4

a width of 10 mm. As shown in Fig. 2(e), CSH_3 had a high fracture strain and high linearity of the stress-strain curve, showing stable mechanical properties. However, the fracture strains of CSH_1 and CSH_2 were small and the linearity of the curve was poor (Table S2 in ESI). Owing to the low surface flatness of the fabric, the yarn force was non-uniform and unstable. The fabric exhibited distinct brittle fracture and poor mechanical properties when a fracture occurred. To further investigate the carbonization process, CSH_1, CSH_2 and CSH_3 were prepared as strain sensors for the tensile strain investigation. As shown in Fig. 2(f), the CSH_3 strain sensor exhibits a much higher tensile strain than CSH_1 and CSH_2. The lower strain was due to the higher brittleness of CSH_1 and CSH_2. CSH_3, which was formed through the gradient heating method, was more flexible and had a higher fracture strain. Therefore, during the stretching process of the CSH_3 strain sensor, the interlacing of more flexible conductive fibers of CSH_3 provided the possibility of a wider strain range. Thus, it can be confirmed that carbonization with gradient heating is more suitable for preparing flexible strain sensors. The thermal decomposition temperature of silk is approximately 303 °C. The insulation conditions of CSH_3 at 350 °C provided an adequate thermal decomposition time and temperature, which helped the habotai to be fully carbonized.

After the gradient heating carbonization process was determined, the carbonization temperature required further investigation. The CSHs were explored and compared at three temperatures, and the SEM images are shown in Fig. 3(a). The average resistances of CSH_3, CSH_4 and CSH_5 were 11.69, 5.12, and 5.08 Ω, respectively, as shown in Fig. S1 (in ESI). Fig. 3(b) demonstrates significant differences in the Raman spectra of CSH_3, CSH_4 and CSH_5, including that the I_D/I_G values at 950 and 1000 °C were lower (0.911 and 0.902, respectively) than 900 °C (0.969). As the temperature increased, the value of I_D/I_G decreased; therefore, the CSHs formed were more fully carbonized and had better electrical conductivity. In the TGA test in Fig. S2 (in ESI), the residual weight after thermal decomposition at 900, 950 and 1000 °C is 24.16%, 23.75% and 23.39%, respectively. It is further proved that the habotai is fully carbonized and converted into more nitrogen-doped carbon materials. All of this explains why the resistance decreases with increasing carbonization temperature. Fig. S3(b) and Table S1 (in ESI) show that CSH_4 has the highest carbon content of 88.3% in the XPS test, and the C content does not change significantly with the increasing temperature. The XRD results are shown in Fig. 3(c). Both wide amorphous peaks in the crystal planes of the graphitic structure are observed. In addition, from the stress-strain curve in Fig. 3(d), it can be seen that CSH_4 and CSH_5 have higher fracture strains, and there is a significant difference in the fracture strain at CSH_3. The CSHs with higher carbonization temperatures exhibit more distinct brittle fractures (Table S2 in ESI). To this end, CSH_3, CSH_4 and CSH_5 strain sensors were prepared for comparison (Fig. 3e). The results show that the CSH_4 strain sensor exhibits a higher tensile strain of 434%. However, the CSH_3 and CSH_5 strain sensors exhibit maximum tensile strains of 197% and 297%, respectively. In summary, the smaller fracture strain of CSH_3 affected the tensile properties of its sensor. Compared with CSH_4, although CSH_5 had a similar fracture strain, the CSH_5 strain sensor was more prone to breaking the conductive network under high tensile strain. This result was due to the difficulty in achieving fiber bridging after the significant brittle fracture of the conductive fibers. To compare the performances of the five CSH strain sensors more concisely and clearly, the maximum tensile strain range, GF, and linearity of the five CSH strain sensors are summarized in Table S3 (in ESI). It can be concluded that the CSH_1 and CSH_2 strain sensors had higher sensitivity in the tensile range, but could not withstand large tensile strengths, which was closely related to the mechanical properties of CSHs. The CSH_4 strain sensor exhibits the best tensile properties with a wide tensile range, high GF, and high linearity. Although the tensile ranges of the CSH_3 and CSH_5 strain sensors are not narrow, their application was limited by their low linearity.

Sensing Performance of the CSH Strain Sensor

To fully analyze the sensing performance of the CSH strain sensor, CSH_4 was chosen as the conductive material to study.

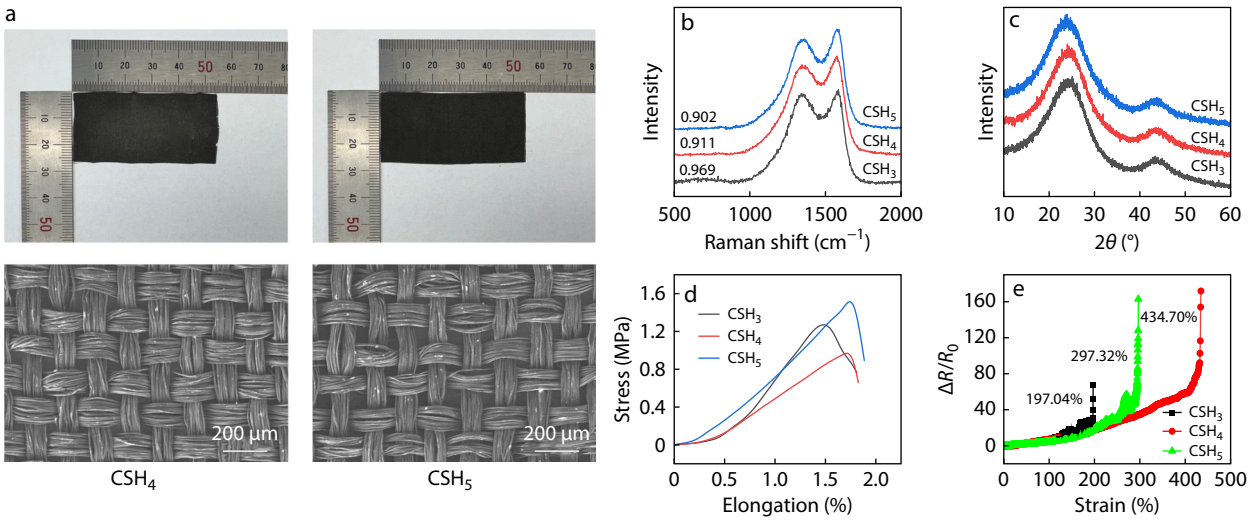

Fig. 3 (a) Photographs and SEM images of CSH_4 and CSH_5; (b) Raman spectra, (c) XRD patterns and (d) stress-strain diagrams of CSH_3, CSH_4 and CSH_5; (e) The relative resistance changes of CSH_3, CSH_4 and CSH_5 strain sensors along the weft direction at a tensile rate of 60 mm·min^{-1}.

https://doi.org/10.1007/s10118-023-2924-4

The CSH_4 strain sensor displays excellent mechanical and electrical performance. Fig. 4(a) shows a cyclic stress-strain curve at 40% strain, where the CSH_4 strain sensor was stretched along the weft direction. The initial curve was slightly different from that of subsequent cycles, with an increase in the repeatability after the third cycle. After 10 cycles, the stress value decreased from 10.60 kPa to 8.68 kPa. The higher stress in the first cycle curve was due to the irreparable fracture of the weft yarn after stretching in CSH_4. The moment of rupture can result in a sudden drop in stress. In the subsequent cycle, CSH_4 no longer exhibited significant fracture, and the stress-strain curve tended to be stable. However, 0%–5% of the strain was stress-free, owing to the plastic deformation caused by the fracture of CSH_4 and relaxation of the elastic matrix. Owing to the high viscoelastic and creep properties of the Ecoflex matrix, the recovery curve lagged behind the tensile curve. To explore the maximum tensile strain of the sensor, a tensile test was performed on the sensor at a tensile rate of 60 mm·min^{-1}. The curve of the relative resistance change ($\Delta R/R_0$) with the strain is shown in Fig. S4 (in ESI). It can be seen intuitively that the maximum tensile strain of the CSH_4 strain sensor increased to 434.7%. The relative resistance of the CSH_4 strain sensor exhibited an increasing linear trend within the applied strain range, and the curve could be divided into two stages. The average GF values of the two processes were calculated by linearly fitting the two curves. In the range of 0%–400%, the GF of the sensor was 14.6, and the linearity was up to 0.959. In the range of 400%–434%, the sensor had a GF of up to 101.4, and the linearity was up to 0.929. When the tensile strain of the sensor was higher than 400%, the internal fabric structure was rapidly destroyed, which resulted in a rapid increase in resistance and the sensor exhibited a higher sensitivity. It was thus definitively proved that the CSH_4 strain sensor had extremely high mechanical properties and linearity, which was helpful for accurate measurement of the sensor under different strains. High linearity facilitated the establishment of a quantitative relation between the change in resistance and the applied strain, which was equivalent. Besides, the high linearity of CSH_4 strain sensor greatly simplified circuit design and data processing compared to multi-range differentiated sensitivity.

Figs. 4(b) and 4(c) show the $\Delta R/R_0$ response of the CSH_4 strain sensor under 5%–400% strain conditions at a tensile rate of 60 mm·min^{-1}. The results indicate that the strain sensor had a clear and accurate $\Delta R/R_0$ at different tensile levels. CSH_4 strain sensors have a robust response even at low

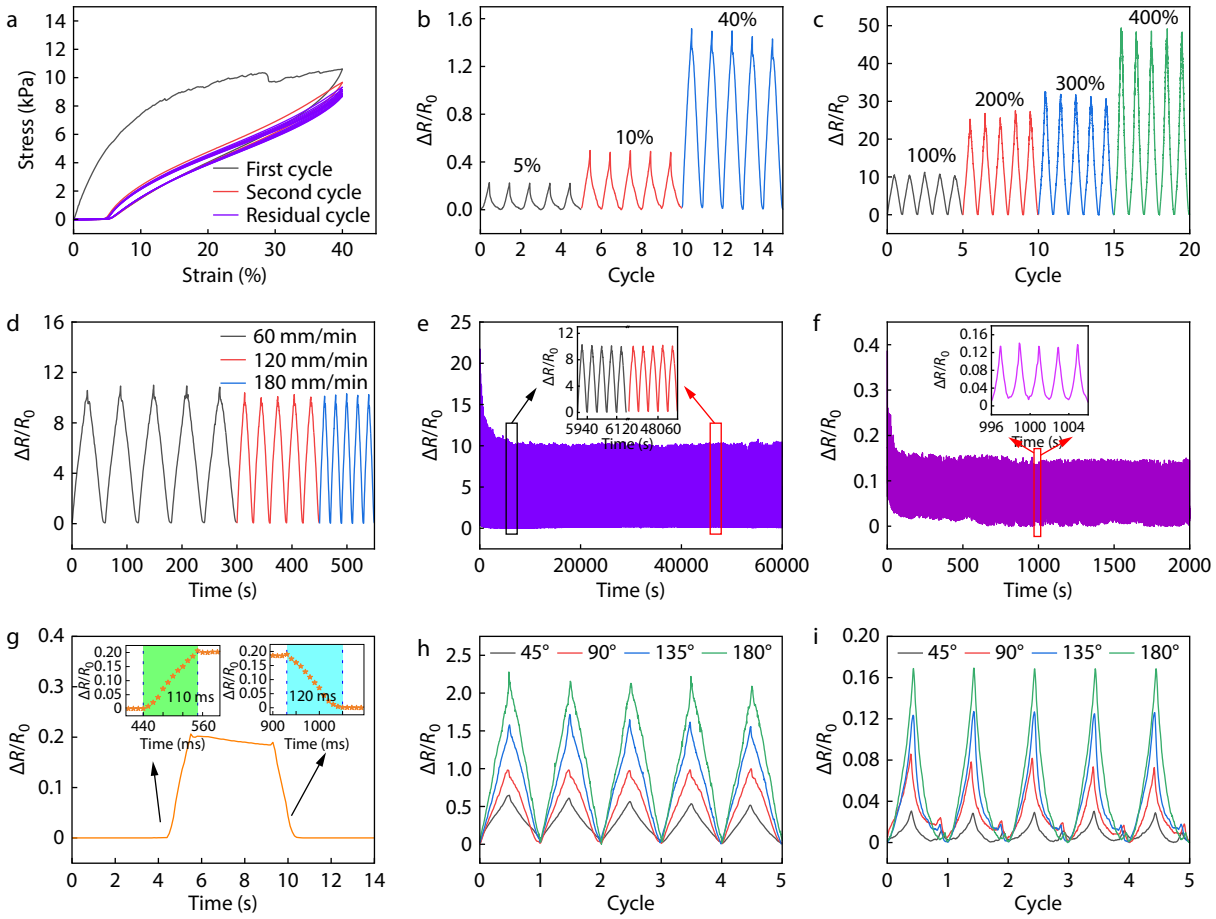

Fig. 4 The performance of the CSH_4 strain sensor. (a) Cyclic stress-strain curves of sensor at a stretching rate of 30 mm·min^{-1}. Tensile response in the strain range of (b) 5%–40% and (c) 100%–400% at a tensile rate of 60 mm·min^{-1}. (d) Relative resistance change at different rates for the same tensile strain (100%). Durability during the 1000 loading-unloading cycles under (e) 100% and (f) 3% tensile strain. (g) The response time and recovery time at a 3.3% tensile strain. (h) CSH_4 strain sensor under different bending angles at a bending rate of 10 (°)·s^{-1}. (i) CSH_4 strain sensor under different torsion angles at a torsion rate of 10 (°)·s^{-1}.

https://doi.org/10.1007/s10118-023-2924-4

strains of 0.1%–1% (Fig. S5 in ESI). Moreover, the sensor demonstrated high repeatability under multiple cycles. The strength of $\Delta R/R_0$ increased proportionally as the strain increased gradually during cyclic stretching. Good stability, repeatability, and linear response of the CSH_4 strain sensor were also observed. In Fig. 4(d), the $\Delta R/R_0$ intensity changes are essentially the same at different tensile rates under 100% tensile strain, indicating that the performance of the sensor was almost independent of the rate. This conclusion has important implications for its practical application in multi-model strains. Therefore, to further explore the durability of the CSH_4 strain sensor under different tensile strains, a load-unload stability test of the sensor was carried out at a rate of 60 mm·min^{-1}. Figs. 4(e) and 4(f) show 1000 cycles of CSH_4 strain-sensor fatigue under large (100%) and small (3%) tensile strains. The excellent continuity, reproducibility, and durability of the sensor were demonstrated over hundreds of stretches and relaxations. However, owing to the high viscoelasticity of the flexible matrix material, a response lag of the coated strain sensor was typically observed, restricting the fast response of the sensor. To this end, a CSH_4 strain sensor was tested for its static response. A 3.3% rapid tensile strain was applied to the sensor using a flexible resistance tester. As shown in Fig. 4(g), the response time of the CSH_4 strain sensor was 110 ms and the recovery time was 120 ms. In addition, when a 100% rapid tensile strain was applied to the CSH4 strain sensor, the response time was 120 ms and the recovery time was 170 ms (Fig. S6 in ESI).

A flexible electronic tester was used to measure the bending of the sensor (Fig. S7 in ESI). In the bending experiment, the sensor was bent along a 1 cm diameter axis body. As shown in Fig. 4(h), when the bending speed is 10 (°)·s^{-1}, it can be found that the $\Delta R/R_0$ intensity of the sensor increases proportionally with the increase of the bending angle (0°–180°). The sensor exhibited a good linear relation (R^2=99.81%) and a sensitivity of 0.67 rad^{-1} over the bending angle range of 0°–180°. As shown in Figs. S8(a)–S8(c) (in ESI), the stability of the CSH_4 strain sensor under different bending strains was demonstrated. After 1000 cycles at 90°, 135° and 180°, $\Delta R/R_0$ remains almost constant, and the sensor exhibits excellent durability and stability.

In addition to the typical tensile and bending strains, torsional strain is another highlight of the CSH_4 strain sensor (Fig. S9 in ESI). The torsion speed was set to 10 (°)·s^{-1} and the selected test range was 0°–180°. Fig. 4(i) clearly shows a positive correlation between the torsion angle and $\Delta R/R_0$. The peak values of $\Delta R/R_0$ were similar in each cycle, and the sensor exhibited good repeatability and a linear response (R^2=96.32%) to torsional strain. The sensor sensitivity was 0.12 rad^{-1}. As shown in Figs. S10(a)–S10(c) (in ESI), angles of 90°, 135° and 180° were chosen to schedule 1000 torsional cyclic fatigue experiments. The results indicated that the overall trend was stable. These results further demonstrate that the CSH_4 strain sensor exhibits excellent reproducibility and stability under different strain models. A solid foundation has thus been laid for the multifunctional composite application of this sensor.

Working Mechanism of the CSH Strain Sensor

Tensile strain was chosen as the analysis model to further explore the strain-sensing mechanism of the sensor. The answer was found in the optical images of the sensor under different strains. As shown in Fig. 5(a), when the sensor was not stretched, CSH_4 presented a tightly arranged plain-weave structure in Ecoflex. The warp yarn and weft yarn did not have fractured parts, and the surface of the sensor was smooth. When the CSH_4 strain sensor was subjected to a tensile strain of 10%, the weft of the CSH_4 broke at its weakest point and tore the adjacent weft (Fig. S11a in ESI). At this stage, weft yarn breakage was the main factor. The warp yarns were subjected to a pulling force, which resulted in a contraction movement that formed a gully. The resistance of the stretched sensor was greater than that of the intact initial conductive network. Since the warp yarn had a small twist, it could fix the weft yarn at the interweaving point with knot. Therefore, weft yarn breakage was more likely to occur at the interweaving point without twist. The weft yarn fracture was not flush. This was due to the loose fibers, weak cohesion force, and no concentrated stress in the yarn, resulting in a weak tearing force of the fibers at the parallel fracture, Therefore the fibers did not tear at the same position. However, some new breaks also appeared in the large interweaving grid. As the strain increased, these new breaks expanded and form significant gullies. When the sensor was stretched to 40%, the gully became wider and more pronounced, but the intact conductive interwoven network in the sensor occupied most of the area (Fig. S11b in ESI). Within the interweaving grid, new weft yarn breaks still appeared, and they would be separated under greater stretch. Under a light microscope, the yarn broke to produce tiny electrically conductive carbon fibers. They were scattered in the matrix "tunnel" and could bridge with each other, still playing an important role in the conductive network. In the meantime, the warp yarn began to slip. It was no longer directly perpendicular to the weft direction, and many S-shaped warp yarns appeared in the fabric structure. The warp yarn appeared loose after being stretched, owing to their high flexibility; this played an important role in sensing large strains with high sensitivity. The loose conductive warp yarns were laid flat in the tunnel, and the few fine fibers began to break under tension. But broken warp yarns were not separated like weft yarns, and bridging was still possible after breakage. With increasing tensile strength, the number of gullies further increased after reaching 100% tensile strength (Fig. S11c in ESI). The area of the conductive interwoven network became significantly smaller and the resistance increased. There were still new weft yarn breaks appeared in the interweaving grid. More conductive short fibers were trapped in the tunnel. It was due to the interaction forces between the fibers and the friction between the fibers and the coating matrix that caused the secondary fracture of the fibers. Under the light microscope, the warp yarn spacing and the number of breaking increased, but adjacent warp yarns could still be connected by the warp and weft interweaving structure. When the tensile strain was increased to 200%, the large interwoven network no longer occupied most of the area and the transparent gullies were more prominent (Fig. S11d in ESI). The old breaks were further stretched apart and new breaks were generated in reduced numbers. More warp yarns were broken under frictional and tensile stresses, which could further lead to an increase in resistance and damage to the conductive network. In addition, the slippage and dispersion of the warp yarns were more pronounced. When the strain was increased to 400%, the weft

https://doi.org/10.1007/s10118-023-2924-4

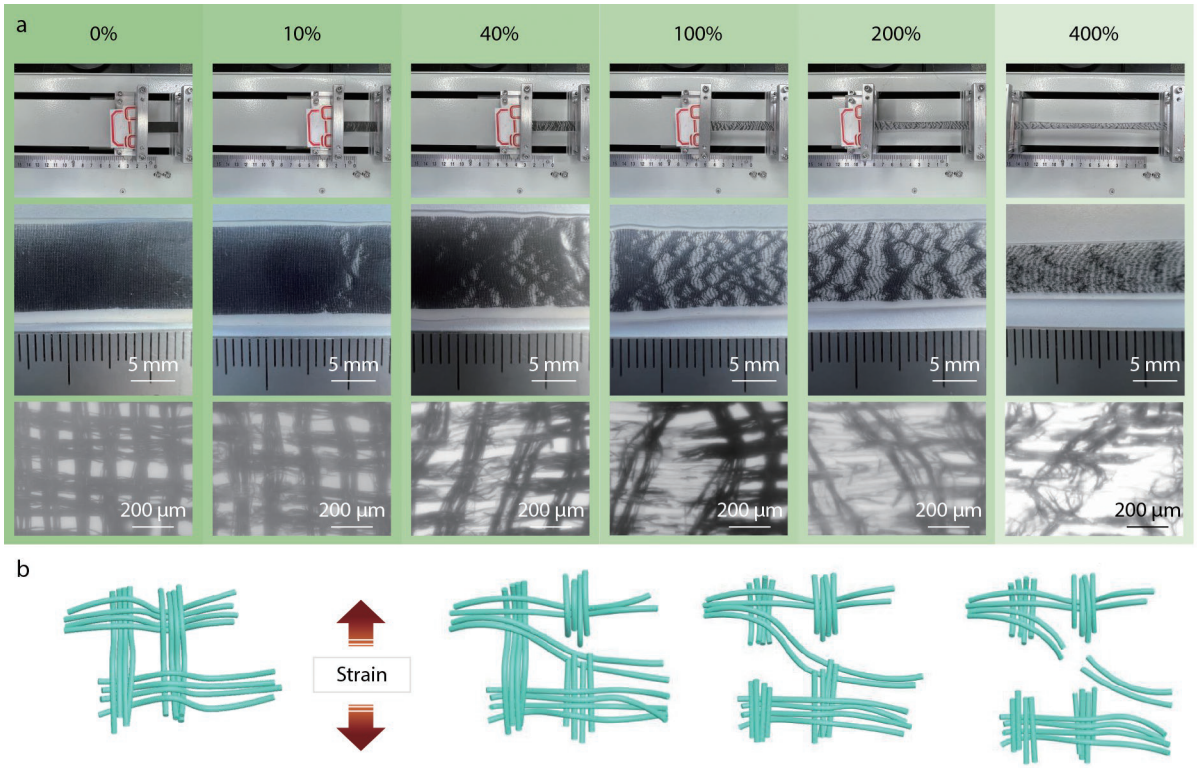

Fig. 5 (a) Photographs and enlarged optical images of CSH_4 strain sensor under different strains of tensile and fracture; (b) Schematic illustration of sensing principle of the CSH_4 strain sensor.

in the stress direction broke (Fig. S11e in ESI). But there were still short wefts that maintain the connection between adjacent warp yarns. The slippage and tilt of the warp made it possible for the sensor to achieve high strain, and the interwoven and bridged weft ensured electrical conductivity between the warp yarns. When the flexible conductive warp was broken, the conductive path was completely disconnected and the sensor failed.

To further explain the increase in the resistance of the CSH_4 strain sensor during stretching, a schematic diagram of the sensor from the initial state to failure is shown in Fig. 5(b). As the tensile strain increases, the weft yarn breaks and then shrinks, driving the warp yarn to separate and tilt. At further increased strains, more weft yarns broke and the tilting of the warp yarns became more pronounced. The conductive path inside the sensor relied more on the tilted warp for conduction. It was not until the warp yarns inside the fabric also broke that the conductive network of the sensor failed and the maximum strain on the sensor was reached.

The bending and tensile strains exhibited similar sensing principles. The bending strain of the shaft would deform the sensor, and the strain direction at each point was tangential to that point. Owing to the appearance of a bending angle, fracture contact and slippage occurred between the small conductive fibers, and an angle was formed between the fibers arranged in parallel contact. At this point, the sensor presented the same "black and white" gully patterns as the tensile strain. With a gradual increase in the bending angle, the contact breaking and slip phenomenon of the internal fibers became increasingly intense, and the transverse fracture of the conductive network promoted the differential change in resistance. The more obvious the gully phenomenon, the higher was the relative resistance of the sensor. The sensor state gradually recovered when the bending angle decreased.

For torsion, the sensor was rotated to form a cylindrical structure. The sides of the flexible sensor were stretched and twisted while the yarn at the central axis was rotated. Therefore, the greater the weft was at the edge of the sensor, the more likely it was to be stretched and torn, forming a trapezoidal shape with wide edges and a narrow middle. As the torsion angle increased, the tension became more prominent and the disconnection of the conductive yarn at the edge further promoted an increase in $\Delta R/R_0$. However, when the tensile force of the torsional transformation was applied to the edge of the sensor, a contraction stress also appeared. The contraction stress would be transferred internally, further acting on the central axis and causing compression. This caused the middle yarn to squeeze and hold more tightly, promoting a tight arrangement of the conductive network. Thus, despite the fracture strain produced by edge stretching during torsion, the tight conductive network in the middle remains compact and intact. This explains why the CSH_4 strain sensor still exhibited a low $\Delta R/R_0$ variation at a high strain of 180°.

Application of Human Motion Monitoring

The highly-strain-tolerant and ultra-sensitive CSH_4 strain sensor can accurately detect human motion and physiological signals. The CSH_4 strain sensor can also distinguish small gaps in motion. We embedded the CSH_4 strain sensor in a pillow (Fig. 6a) and monitored the head movements of a volunteer using it.

https://doi.org/10.1007/s10118-023-2924-4

When the volunteer quickly lowered her head, the $\Delta R/R_0$ of the sensor increased rapidly and then leveled off. When the volunteer raised her head, the head exerted a small tensile deformation on the pillow owing to the support force generated from the waist, and $\Delta R/R_0$ showed a second small spike (Fig. 6b) the waist will support and exert force, which drives the head to produce a slight downward pressure deformation on the pass pillow. When the volunteer's head was placed on the pillow, a wide left-right swing still produced a significant $\Delta R/R_0$ (Fig. 6c), proving that the CSH_4 strain sensor could withstand and monitor large deformations caused by human movement. In addition, the CSH_4 strain sensor could also detect subtle physiological activity. Breathing of the human body after lying down drives a slight movement of the head. When the volunteer inhaled, the head sank slightly, creating a pressure strain on the sensor, while when she exhaled, the head relaxed and rose, and the sensor strain recovered. Thus, a minor breathing signal could be visibly detected when the volunteer breathed while lying on the pillow (Fig. 6d). The CSH_4 strain sensor could detect large and slight deformations and distinguish small differences in deformation, such as different sleeping positions. When a human sleep, the head and pillow contact is divided into two types: the back of the head and pillow contact (supine sleep) and the side of the head and pillow contact (side sleep). Because the human head is not a regular sphere, supine and side sleep generally have different contact areas with the pillow. For example, the volunteer slept on her back with less contact area with the pillow. $\Delta R/R_0$ was recorded directly after the volunteers laid down in two ways (Fig. 6e). In the relaxed state, $\Delta R/R_0$ was higher when the volunteer supine slept and the deformation of the head against the pillow was greater. In contrast, the deformation during side sleeping was relatively small, and $\Delta R/R_0$ was smaller. This experiment demonstrated the excellent sensitivity and perception of the sensor. By analogy, CSH_4 strain sensors may be widely used in various situations.

Air pollution directly impacts human health. In recent years, the number of patients with respiratory disease has increased. However, the monitoring of sleep status is limited to wearable devices such as smart wristbands and the wearing of these devices may increase the stress burden on patients. Therefore, the research and innovation of smart pillows are of great significance. There is no precedent for the development of smart pillows. The invented smart pillow can clearly and precisely detect physiological states, greatly eliminate the requirement for wearing devices, and put forward new ideas and creations for development within the intelligent health domain. The smart pillow was designed to monitor sleep throughout the entire process, allowing the movement of the subject's head to be clearly recorded during sleep. The physiological status of monitored patients after sleep can be determined according to the breathing frequency and amplitude. For patients with dyspnea, it can be determined whether there is shortness of breath or difficulty sleeping. In addition, the sleeping position can be accurately identified to help regulate the sleeping position. Through simple comparative analysis of the signals, the sleep quality of patients can be judged and also provide an auxiliary basis for doctors to judge the patient's condition.

CSH_4 strain sensors are able to detect all kinds of small and intense activities outstandingly. Therefore, it is suitable for monitoring and improving human motor activity. In table tennis, the critical body parts are the wrist, elbow, shoulder, knees and feet. However, improper training can lead to pos-

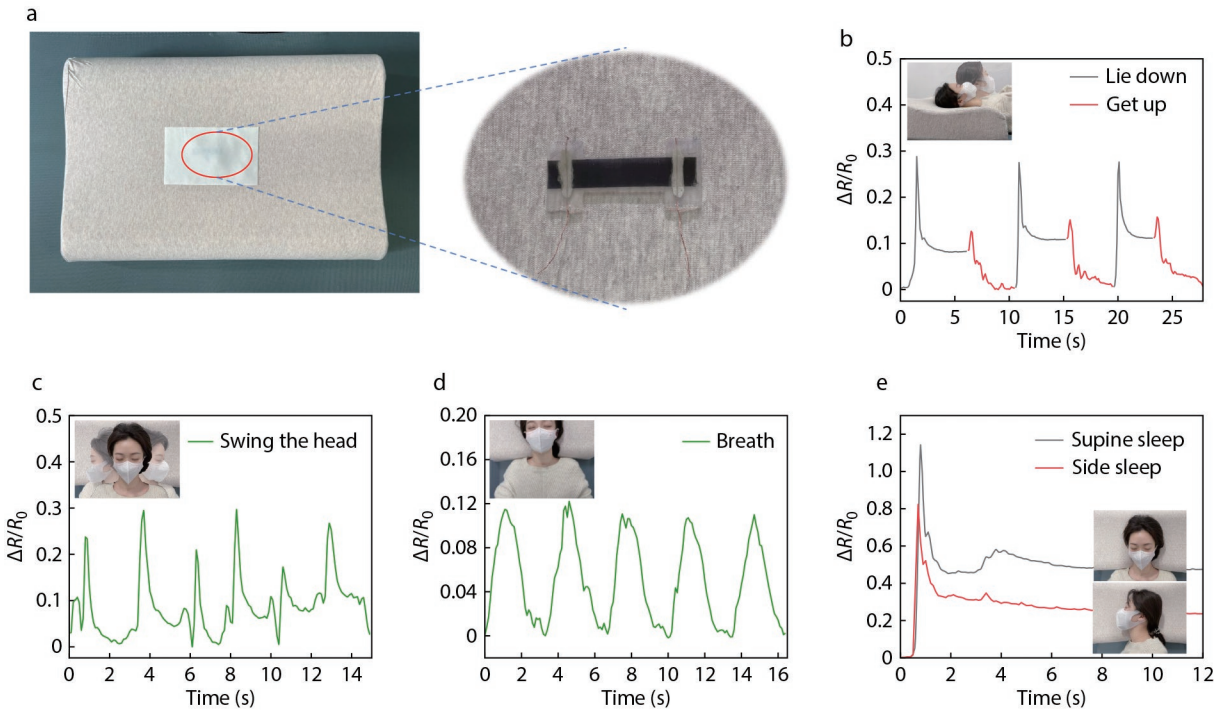

Fig. 6 (a) Schematic diagram of the smart pillow. Application of the smart pillow during (b) lying down and getting up, (c) swinging of the head, (d) breathing, (e) supine and side sleeping.

https://doi.org/10.1007/s10118-023-2924-4

tural distortion and joint damage. Therefore, a standard and quantitative movement is particularly important, and CSH_4 strain sensors were used to achieve detection at key locations. The sensor was attached to the wrist strap. The topspin was powered by a quick twist of the volunteer's wrist, which deformed the wristband (Figs. 7a and 7d). $\Delta R/R_0$ increased in response to the volunteers' topspin. The volunteers' hands gradually returned to the initial position after serving, and $\Delta R/R_0$ decreased and returned to the initial value. When volunteers hit a forehand attack or backhand block, they were required to wave their arms to achieve the effect of hitting the ball. The speed and bending of the elbow determined the speed and direction of rebound of the table tennis ball (Figs. 7b and 7e). We tested the speed of the volunteer's elbow when hitting the ball at different velocities. Sensors can effectively maintain and monitor large deformations of the human body. Movements in the shoulder (Figs. 7c and 7f)), Achilles tendon (Figs. 7g and 7h), and knee (Figs. 7h and 7i) were also clearly identified. To highlight the advantages of the sensor in detecting the entire movement process, we attached it to the elbow and selected four classic table tennis movements for two consecutive experiments (forehand rub, backhand rub, forehand attack, and backhand block). As shown in Fig. 7(j), the CSH_4 strain sensor perfectly presented a complete movement flow with high reproducibility and specificity. By analyzing the amplitude and frequency of the $\Delta R/R_0$ images, it was helpful to control the amount of exercise and prevent body sprain. They may also be used for the training and calibration of table tennis play. By comparing the movement signals of students with those of professional ath-

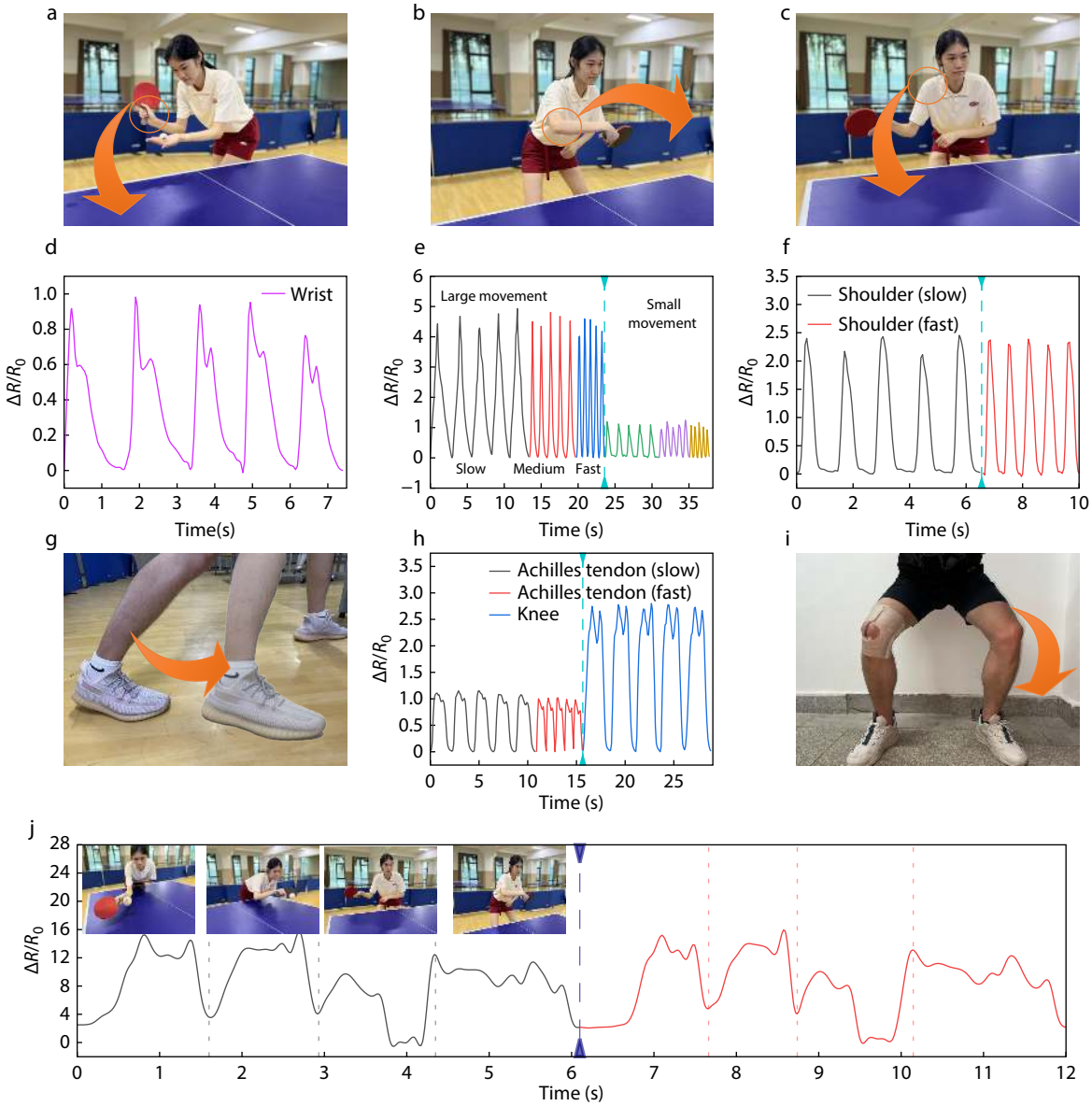

Fig. 7 The wearable CSH_4 strain sensor used to detect table tennis movement, with motion photos at (a) wrist, (b) elbow, (c) shoulder, (g) achilles tendon and (i) knee. Corresponding signal images of (d) wrist twisting, (e) elbow bending, (f) shoulder movement, (h) Achilles tendon stretching and knee bending. (j) Four sequential movements of forehand rub, backhand rub, forehand attack and backhand block.

https://doi.org/10.1007/s10118-023-2924-4

letes, personalized, intelligent, and scientific table tennis teaching and training could be realized to improve exercise efficiency in a more personalized way.

CONCLUSIONS

In summary, a multi-model deformation and ultrasensitive flexible strain sensor based on CSHs was successfully prepared. Habotai achieved a perfect transition from an insulating material to a high-performance sensor by carbonization. The effects of the heating rates, heating schedules, and carbonization temperatures on the CSHs were carefully explored. It was determined that CSHs could obtain the best performance under the process conditions of gradient heating up to 950 °C. The CSH_4 strain sensor could withstand a maximum tensile strain of 434%. GFs of the CSH_4 strain sensors were 14.6 in the tensile range of 400% with a linearity of 0.959. CSH_4 strain sensors had an extremely fast response time (approximately 110 ms) and recovery time (approximately 120 ms). The sensor could also detect bending strain at an angle of 0°–180° and torsional strain at an angle of 0°–180° with high sensitivity. Moreover, good stability and repeatability were achieved under the multi-model strain conditions. A new type of smart pillow was developed for the first time, which fully demonstrated the practicality of the CSH_4 strain sensor. It can accurately record the various movements of the human head during sleep, and the breathing status can also be accurately identified. In addition, the CSH_4 strain sensor could easily detect and analyze table tennis movements in multiple parts, which was helpful for improving player proficiency in table tennis.

Conflict of Interests

The authors declare no interest conflict.

Electronic Supplementary Information

Electronic supplementary information (ESI) is available free of charge in the online version of this article at http://doi.org/10.1007/s10118-023-2924-4.

ACKNOWLEDGMENTS

This work was financially supported in part by the Jiangsu Provincial Key Research and Development Program (No. BE2019045); in part by the Third-Priority Academic Program Development of Jiangsu Higher Education Institutions; in part by the Opening Project of National Engineering Laboratory for Modern Silk, Soochow University (No. SDGC2245); in part by the Postgraduate Research & Practice Innovation Program of Jiangsu Province (No. KYCX21_2958); and Qing Lan Project.

REFERENCES

1 Amjadi, M.; Kyung, K. U.; Park, I.; Sitti, M. Stretchable, skin-mountable, and wearable strain sensors and their potential applications: a review. *Adv. Funct. Mater.* **2016**, *26*, 1678–1698.
2 Wu, Y. T.; Yan, T.; Pan, Z. J. Wearable carbon-based resistive sensors for strain detection: a review. *IEEE Sens. J.* **2021**, *21*, 4030–4043.
3 Goldoni, R.; Ozkan-Aydin, Y.; Kim, Y. S.; Kim, J.; Zavanelli, N.; Mahmood, M.; Liu, B.; Hammond, F. L., 3rd; Goldman, D. I.; Yeo, W. H. Stretchable nanocomposite sensors, nanomembrane interconnectors, and wireless electronics toward feedback-loop control of a soft earthworm robot. *ACS Appl. Mater. Interfaces* **2020**, *12*, 43388–43397.
4 Zhang, M.; Wang, C.; Wang, Q.; Jian, M.; Zhang, Y. Sheath-core graphite/silk fiber made by dry-meyer-rod-coating for wearable strain sensors. *ACS Appl. Mater. Interfaces* **2016**, *8*, 20894–20899.
5 Hang, C. Z.; Zhao, X. F.; Xi, S. Y.; Shang, Y. H.; Yuan, K. P.; Yang, F.; Wang, Q. G.; Wang, J. C.; Zhang, D. W.; Lu, H. L. Highly stretchable and self-healing strain sensors for motion detection in wireless human-machine interface. *Nano Energy* **2020**, *76*, 105064.
6 Tian, H.; Shu, Y.; Cui, Y. L.; Mi, W. T.; Yang, Y.; Xie, D.; Ren, T. L. Scalable fabrication of high-performance and flexible graphene strain sensors. *Nanoscale* **2014**, *6*, 699–705.
7 Yan, T.; Wu, Y.; Pan, Z. Anisotropy of resistance-type strain sensing networks based on aligned carbon nanofiber membrane. *J Mater. Sci.* **2021**, *56*, 6292–6305.
8 Zhao, M.; Li, D.; Huang, J.; Wang, D.; Mensah, A.; Wei, Q. A multifunctional and highly stretchable electronic device based on silver nanowire/wrap yarn composite for a wearable strain sensor and heater. *J. Mater. Chem. C* **2019**, *7*, 13468–13476.
9 Zhang, J.; Wan, L.; Gao, Y.; Fang, X.; Lu, T.; Pan, L.; Xuan, F. Highly stretchable and self-healable mxene/polyvinyl alcohol hydrogel electrode for wearable capacitive electronic skin. *Adv. Electron. Mater.* **2019**, *5*, 1900285.
10 Cai, L.; Song, L.; Luan, P.; Zhang, Q.; Zhang, N.; Gao, Q.; Zhao, D.; Zhang, X.; Tu, M.; Yang, F.; Zhou, W.; Fan, Q.; Luo, J.; Zhou, W.; Ajayan, P. M.; Xie, S. Super-stretchable, transparent carbon nanotube-based capacitive strain sensors for human motion detection. *Sci. Rep.* **2013**, *3*, 3048.
11 Yang, J. C.; Kim, J. O.; Oh, J.; Kwon, S. Y.; Sim, J. Y.; Kim, D. W.; Choi, H. B.; Park, S. Microstructured porous pyramid-based ultrahigh sensitive pressure sensor insensitive to strain and temperature. *ACS Appl. Mater. Interfaces* **2019**, *11*, 19472–19480.
12 Liu, Y.; Hu, Y.; Zhao, J.; Wu, G.; Tao, X.; Chen, W. Self-powered piezoionic strain sensor toward the monitoring of human activities. *Small* **2016**, *12*, 5074–5080.
13 Qian, S.; Qin, L.; He, J.; Zhang, N.; Qian, J.; Mu, J.; Geng, W.; Hou, X.; Chou, X. A lead-free stretchable piezoelectric composite for human motion monitoring. *Mater. Lett.* **2020**, *261*, 127119.
14 Meng, B.; Tang, W.; Too, Z. H.; Zhang, X.; Han, M.; Liu, W.; Zhang, H. A transparent single-friction-surface triboelectric generator and self-powered touch sensor. *Energy Environ. Sci.* **2013**, *6*, 3235–3240.
15 Wang, S. H.; Lin, L.; Wang, Z. L. Triboelectric nanogenerators as self-powered active sensors. *Nano Energy* **2015**, *11*, 436–462.
16 Gao, Y.; Guo, F.; Cao, P.; Liu, J.; Li, D.; Wu, J.; Wang, N.; Su, Y.; Zhao, Y. Winding-locked carbon nanotubes/polymer nanofibers helical yarn for ultrastretchable conductor and strain sensor. *ACS Nano* **2020**, *14*, 3442–3450.
17 Ding, L.; Xuan, S.; Feng, J.; Gong, X. Magnetic/conductive composite fiber: a multifunctional strain sensor with magnetically driven property. *Compos. Part A* **2017**, *100*, 97–105.
18 Tang, J.; Wu, Y.; Ma, S.; Yan, T.; Pan, Z. Flexible strain sensor based on CNT/TPU composite nanofiber yarn for smart sports bandage. *Compos. Part B Eng.* **2022**, *232*, 109605.
19 Ma, S. D.; Tang, J.; Yan, T.; Pan, Z. J. Performance of flexible strain sensors with different transition mechanisms: a review. *IEEE Sens. J.* **2022**, *22*, 7475–7498.
20 Tang, J.; Wu, Y.; Ma, S.; Yan, T.; Pan, Z. Strain-sensing composite nanofiber filament and regulation mechanism of shoulder peaks based on carbon nanomaterial dispersion. *ACS Appl. Mater. Interfaces* **2023**, *15*, 7329–7404.

21 Wu, Y.; Yan, T.; Zhang, K.; Pan, Z. A hollow core-sheath composite fiber based on polyaniline/polyurethane: preparation, properties, and multi-model strain sensing performance. *Adv. Mater. Technol.* **2023**, *8*, 2200777.
22 Park, J. J.; Hyun, W. J.; Mun, S. C.; Park, Y. T.; Park, O. O. Highly stretchable and wearable graphene strain sensors with controllable sensitivity for human motion monitoring. *ACS Appl. Mater. Interfaces* **2015**, *7*, 6317–6324.
23 Cai, Y.; Shen, J.; Ge, G.; Zhang, Y.; Jin, W.; Huang, W.; Shao, J.; Yang, J.; Dong, X. Stretchable $Ti_3C_2T_x$ MXene/carbon nanotube composite based strain sensor with ultrahigh sensitivity and tunable sensing range. *ACS Nano* **2018**, *12*, 56–62.
24 Yee, M. J.; Mubarak, N. M.; Abdullah, E. C.; Khalid, M.; Walvekar, R.; Karri, R. R.; Nizamuddin, S.; Numan, A. Carbon nanomaterials based films for strain sensing application-a review. *Nano-Struct. Nano-Object* **2019**, *18*, 100312.
25 Huang, J.; Li, D.; Zhao, M.; Mensah, A.; Lv, P.; Tian, X.; Huang, F.; Ke, H.; Wei, Q. Highly sensitive and stretchable CNT-bridged AgNP strain sensor based on TPU electrospun membrane for human motion detection. *Adv. Electron. Mater.* **2019**, *1900241*, 5.
26 Sang, S.; Liu, L.; Jian, A.; Duan, Q.; Ji, J.; Zhang, Q.; Zhang, W. Highly sensitive wearable strain sensor based on silver nanowires and nanoparticles. *Nanotechnology* **2018**, *29*, 255202.
27 Li, M.; Li, H.; Zhong, W.; Zhao, Q.; Wang, D. Stretchable conductive polypyrrole/polyurethane (PPy/PU) strain sensor with netlike microcracks for human breath detection. *ACS Appl. Mater. Interfaces* **2014**, *6*, 1313–1319.
28 Gong, X. X.; Fei, G. T.; Fu, W. B.; Fang, M.; Gao, X. D.; Zhong, B. N.; Zhang, L. D. Flexible strain sensor with high performance based on PANI/PDMS films. *Org. Electron.* **2017**, *47*, 51–56.
29 Jia, Y.; Shen, L.; Liu, J.; Zhou, W.; Du, Y.; Xu, J.; Liu, C.; Zhang, G.; Zhang, Z.; Jiang, F. An efficient PEDOT-coated textile for wearable thermoelectric generators and strain sensors. *J. Mater. Chem. C* **2019**, *7*, 3496–3502.
30 Tran Quang, T.; Lee, N. E. Flexible and stretchable physical sensor integrated platforms for wearable human-activity monitoring and personal healthcare. *Adv. Mater.* **2016**, *28*, 4338–4372.
31 Tang, J.; Wu, Y.; Ma, S.; Yan, T.; Pan, Z. Sensing mechanism of a flexible strain sensor developed directly using electrospun composite nanofiber yarn with ternary carbon nanomaterials. *iScience* **2022**, *25*, 105162.
32 Ma, D. L.; Ma, Y.; Chen, Z. W.; Hu, A. M. A silk fabric derived carbon fibre net for transparent capacitive touch pads and all-solid supercapacitors. *J. Mater. Chem. A* **2017**, *5*, 20608–20614.
33 Pan, P.; Hu, Y.; Wu, K.; Cheng, Z.; Shen, Z.; Jiang, L.; Mao, J.; Ni, C.; Ge, Y.; Wang, Z. Growth of $ZnCo_2O_4$ nanocubes on flexible biochar substrate derived from natural silk waste fabric for lithium-ion battery anode. *J. Alloys. Compd.* **2020**, *814*, 152306.
34 Li, X.; Zhao, J.; Cai, Z.; Ge, F. Free-standing carbon electrode materials with three-dimensional hierarchically porous structure derived from waste dyed silk fabrics. *Mater. Res. Bull.* **2018**, *107*, 355–360.
35 Li, X.; Sun, C.; Cai, Z.; Ge, F. High-performance all-solid-state supercapacitor derived from PPy coated carbonized silk fabric. *Appl. Surf. Sci.* **2019**, *473*, 967–975.
36 Chen, C.; Ran, R.; Yang, Z.; Lv, R.; Shen, W.; Kang, F.; Huang, Z. H. An efficient flexible electrochemical glucose sensor based on carbon nanotubes/carbonized silk fabrics decorated with Pt microspheres. *Sens. Actuators B* **2018**, *256*, 63–70.
37 Ji, W.; Wu, D.; Tang, W.; Xi, X.; Su, Y.; Guo, X.; Liu, R. Carbonized silk fabric-based flexible organic electrochemical transistors for highly sensitive and selective dopamine detection. *Sens. Actuators B* **2020**, *304*, 127414.
38 Martel, A.; Burghammer, M.; Davies, R. J.; Riekel, C. Thermal behavior of bombyx mori silk: evolution of crystalline parameters, molecular structure, and mechanical properties. *Biomacromolecules* **2007**, *8*, 3548–3556.
39 Xiong, X.; Tang, Y.; Xu, C.; Huang, Y.; Wang, Y.; Fu, L.; Lin, C.; Zhou, D.; Lin, Y. High carbonization temperature to trigger enzyme mimicking activities of silk-derived nanosheets. *Small* **2020**, *16*, e2004129.
40 Li, X.; Zhao, J.; Cai, Z.; Ge, F. A dyeing-induced heteroatom-co-doped route toward flexible carbon electrode derived from silk fabric. *J. Mater. Sci.* **2018**, *53*, 7735–7743.
41 Hu, M.; Hu, T.; Cheng, R.; Yang, J.; Cui, C.; Zhang, C.; Wang, X. MXene-coated silk-derived carbon cloth toward flexible electrode for supercapacitor application. *J. Energy Chem.* **2018**, *27*, 161–166.
42 Huang, P.; Yu, X. G.; Li, Y. Q.; Fu, Y. F.; Gan, D. M.; Taha, T.; Fu, Y. Q.; Hu, N.; Fu, S. Y. Architectural design of flexible anisotropic piezoresistive composite for multiple-loading recognization. *Compos. B. Eng.* **2020**, *182*, 107631.
43 Deng, C.; Pan, L.; Cui, R.; Li, C.; Qin, J. Wearable strain sensor made of carbonized cotton cloth. *J. Mater. Sci.: Mater. Electron.* **2016**, *28*, 3535–3541.
44 Liu, Z.; Chen, K.; Fernando, A.; Gao, Y.; Li, G.; Jin, L.; Zhai, H.; Yi, Y.; Xu, L.; Zheng, Y.; Li, H.; Fan, Y.; Li, Y.; Zheng, Z. Permeable graphited hemp fabrics-based, wearing-comfortable pressure sensors for monitoring human activities. *Chem. Eng. J.* **2021**, *403*, 126191.
45 Liang, J. J.; Zhao, Z. B.; Tang, Y. C.; Liang, Z. H.; Sun, L. L.; Pan, X.; Wang, X. Z.; Qiu, J. S. A wearable strain sensor based on carbon derived from linen fabrics. *New Carbon Mater.* **2020**, *35*, 522–530.
46 Wang, C.; Zhang, M.; Xia, K.; Gong, X.; Wang, H.; Yin, Z.; Guan, B.; Zhang, Y. Intrinsically stretchable and conductive textile by a scalable process for elastic wearable electronics. *ACS Appl. Mater. Interfaces* **2017**, *9*, 13331–13338.
47 Zhang, M.; Wang, C.; Wang, H.; Jian, M.; Hao, X.; Zhang, Y. Carbonized cotton fabric for high-performance wearable strain sensors. *Adv. Funct. Mater.* **2017**, *27*, 1604795.
48 Yan, T.; Zhou, H.; Niu, H.; Shao, H.; Wang, H.; Pan, Z.; Lin, T. Highly sensitive detection of subtle movement using a flexible strain sensor from helically wrapped carbon yarns. *J. Mater. Chem. C* **2019**, *7*, 10049–10058.
49 Wang, C.; Xia, K.; Jian, M.; Wang, H.; Zhang, M.; Zhang, Y. Carbonized silk georgette as an ultrasensitive wearable strain sensor for full-range human activity monitoring. *J. Mater. Chem. C* **2017**, *5*, 7604–7611.
50 Wang, C.; Li, X.; Gao, E.; Jian, M.; Xia, K.; Wang, Q.; Xu, Z.; Ren, T.; Zhang, Y. Carbonized silk fabric for ultrastretchable, highly sensitive, and wearable strain sensors. *Adv. Mater.* **2016**, *28*, 6640–6648.
51 Chen, Z.; Yan, T.; Pan, Z. Review of flexible strain sensors based on cellulose composites for multi-faceted applications. *Cellulose* **2021**, *28*, 615–645.
52 Rousseau, M. E.; Lefevre, T.; Beaulieu, L.; Asakura, T.; Pezolet, M. Study of Protein conformation and orientation in silkworm and spider silk fibers using Raman microspectroscopy. *Biomacromolecules* **2004**, *5*, 2247–2257.
53 Belin, T.; Epron, F. Characterization methods of carbon nanotubes: a review. *J. Mater. Sci. Eng. B* **2005**, *119*, 105–118.
54 Atchudan, R.; Edison, T. N. J. I.; Chakradhar, D.; Perumal, S.; Shim, J. J.; Lee, Y. R. Facile green synthesis of nitrogen-doped carbon dots using chionanthus retusus fruit extract and investigation of their suitability for metal ion sensing and biological applications. *Sens. Actuators B* **2017**, *246*, 497–509.

https://doi.org/10.1007/s10118-023-2924-4